

# Engineering Perovskite Bandgap for Control of Hot-Electron Dynamics in Plasmonic Nanodiodes

Yujin Park, Jungkweon Choi, Daehan Kim, Jungmin Kim, Yujin Roh, Hyunhwa Lee, Dae Won Cho, Byungha Shin,\* Hyotcherl Ihee,\* and Jeong Young Park\*

Despite extensive research on utilizing plasmonic hot carriers to advance photovoltaics and photocatalysts, achieving high hot-carrier flux remains challenging due to their rapid relaxation. Recent studies have shown that combining plasmonic metals with perovskites improves hot-electron flow, due to the slow hot-electron relaxation in perovskites. Additionally, perovskites offer the advantage of facile bandgap tuning through composition changes. Herein, the influence of tuning the perovskite bandgap on the lifetime and flow of hot electrons in a perovskite/plasmonic Au/TiO<sub>2</sub> nanodiode is explored. The findings reveal that perovskites with wider bandgaps exhibit improved hot-electron lifetime and flow, attributed to the modified hot-electron energy favoring a slower energy loss rate, as verified by ultrafast transient absorption spectroscopic analysis. It is believed that the results successfully demonstrate the integration of engineered hot-carrier physics into device functions, providing valuable guidance for the design of optimized hot-carrier-based devices in the future.

carriers has emerged as an essential task for developing efficient photovoltaics because a significant portion of the absorbed photon energy is dissipated through the hot-carrier relaxation process.<sup>[7]</sup> Unfortunately, collecting sufficient hot carriers for practical applications is challenging, due to the ultrafast hot-carrier relaxation dynamics. To address this issue, two approaches have been proposed: enhancing hot-carrier density and extending hot-carrier lifetime. The former approach can be realized using plasmonic metals, which strongly interact with incident photons by generating coherent free electron oscillation, called localized surface plasmon resonance (LSPR). The oscillating energy is subsequently transferred to the ground-state carriers to excite hot carriers through Landau damping.<sup>[8]</sup> Simultaneously, the strongly confined *E*-field on the plasmonic metal surface promotes high optical absorption of surrounding materials.<sup>[9,10]</sup> The latter approach can be realized by using materials with slow hot-carrier relaxation dynamics as a photosensitizer. Incidentally, organic–inorganic lead halide perovskites have been shown to be excellent candidates for hot-carrier applications, due to their remarkably long hot-carrier lifetimes compared to other semiconductors, which arise from the hot-phonon bottleneck effect, Auger heating effect, large polaron formation, and band-filling effect.<sup>[7,11]</sup>

## 1. Introduction

Harvesting plasmonic hot carriers using metal–semiconductor structures has been in the limelight for photovoltaics<sup>[1–3]</sup> and photocatalysts,<sup>[4–6]</sup> as it allows us to use a wide spectral range from visible to infrared and achieve strong electric field (*E*-field) enhancement at the nanoscale. In particular, harnessing hot

carriers has emerged as an essential task for developing efficient photovoltaics because a significant portion of the absorbed photon energy is dissipated through the hot-carrier relaxation process.<sup>[7]</sup> Unfortunately, collecting sufficient hot carriers for practical applications is challenging, due to the ultrafast hot-carrier relaxation dynamics. To address this issue, two approaches have been proposed: enhancing hot-carrier density and extending hot-carrier lifetime. The former approach can be realized using plasmonic metals, which strongly interact with incident photons by generating coherent free electron oscillation, called localized surface plasmon resonance (LSPR). The oscillating energy is subsequently transferred to the ground-state carriers to excite hot carriers through Landau damping.<sup>[8]</sup> Simultaneously, the strongly confined *E*-field on the plasmonic metal surface promotes high optical absorption of surrounding materials.<sup>[9,10]</sup> The latter approach can be realized by using materials with slow hot-carrier relaxation dynamics as a photosensitizer. Incidentally, organic–inorganic lead halide perovskites have been shown to be excellent candidates for hot-carrier applications, due to their remarkably long hot-carrier lifetimes compared to other semiconductors, which arise from the hot-phonon bottleneck effect, Auger heating effect, large polaron formation, and band-filling effect.<sup>[7,11]</sup>

In this context, a perovskite plasmonic nanodiode has shown the synergistic effect of combining plasmonic metal and lead halide perovskite, enhancing both hot-electron flow and lifetime.<sup>[12]</sup> This synergistic effect of simultaneous excitation of LSPR and hot carriers in perovskites arises from the amplified hot-carrier generation in plasmonic metal via LSPR dephasing and increased hot-carrier generation in perovskite from the confined *E*-field on the plasmonic metal surface. Additionally, the 3D Schottky barrier interface between perovskite (PVSK) and plasmonic Au promotes hot-carrier injection. Subsequent studies, including those on MAPbI<sub>3</sub>-plasmonic Ag Schottky nanodiode<sup>[13]</sup> and MAPbI<sub>3</sub>-Au nanoprism photodetectors,<sup>[14]</sup> supported the idea that the interplay of plasmonic metal and perovskites is beneficial to improve hot-carrier flows. While the boosting of hot-carrier lifetime and flux through the combination of perovskite and plasmonic metal is well established, the enhancement of hot-carrier lifetime and flow within the perovskite material itself remains elusive. Although a few studies using ultrafast time-resolved spectroscopy showed the feasibility of controlling

Y. Park, J. Choi, J. Kim, Y. Roh, H. Lee, D. W. Cho, H. Ihee, J. Y. Park  
Department of Chemistry  
Korea Advanced Institute of Science and Technology (KAIST)  
Daejeon 34141, Republic of Korea  
E-mail: hyotcherl.ihee@kaist.ac.kr; jeongyoungpark@kaist.ac.kr

Y. Park, J. Choi, J. Kim, D. W. Cho, H. Ihee  
Center for Advanced Reaction Dynamics  
Institute for Basic Science (IBS)  
Daejeon 34141, Republic of Korea

J. Choi, J. Kim, H. Ihee  
KI for the BioCentury  
Korea Advanced Institute of Science and Technology (KAIST)  
Daejeon 34141, Republic of Korea

D. Kim, B. Shin  
Department of Materials Science and Engineering  
Korea Advanced Institute of Science and Technology (KAIST)  
Daejeon 34141, Republic of Korea  
E-mail: byungha@kaist.ac.kr

 The ORCID identification number(s) for the author(s) of this article can be found under <https://doi.org/10.1002/solr.202400433>.

DOI: 10.1002/solr.202400433

hot-carrier lifetime of perovskites by modifying chemical composition,<sup>[15,16]</sup> most research has focused on thick films (100 nm or more). These thick films exceed the mean-free path of hot carriers of perovskite and do not provide a clear understanding of hot-carrier extraction beyond the relaxation mechanism. Furthermore, little effort has been devoted to experimentally demonstrating how the hot-electron-driven photocurrent changes due to the altered hot-electron dynamics in PVSK. Incidentally, modifying the halide compositions of perovskites allows for the tuning of their bandgaps,<sup>[17]</sup> which is a crucial aspect for achieving multijunction solar cells,<sup>[18]</sup> while the correlation between bandgap tuning and changes in hot-carrier dynamics has not been extensively studied.

In this study, we demonstrate the impact of engineering perovskite bandgap to improve the hot-carrier lifetime and flow. We utilize a perovskite/plasmonic Au/TiO<sub>2</sub> Schottky nanodiode as our experimental platform to assess changes in hot-electron flow across various perovskite bandgaps. Our findings demonstrate that perovskites with wider bandgaps result in highly enhanced incident photon-to-current conversion efficiency (IPCE) due to increased hot-electron flow in the perovskites. Additionally, our femtosecond transient absorption (TA) spectroscopy analysis reveals the origin of the enhanced hot-electron flux in wider perovskite bandgaps, attributing it to elongated hot-electron lifetimes. Building on these comprehensive observations of improved hot-electron flow and elongated hot-electron lifetime through perovskite bandgap modification, we explain the extended hot-electron lifetime with wider bandgaps is associated with the generation of hot electrons with relatively low excess energy, resulting in slower scattering rate.

## 2. Results and Discussions

### 2.1. Characterizations of Perovskite Plasmonic Nanodiodes

To explore the hot-carrier dynamics of perovskite in relation to its bandgap, we fabricated perovskite-modified plasmonic Au nanodiode to observe hot-electron flow as the steady-state current (Figure 1a). An active area (2 mm × 2 mm) comprises perovskite, plasmonic Au, and TiO<sub>2</sub> thin layers. Perovskites based on (FA<sub>0.65</sub>MA<sub>0.20</sub>CS<sub>0.15</sub>)Pb(I<sub>1-x</sub>Br<sub>x</sub>)<sub>3</sub>, X = 0, 0.2, 0.4, were prepared, and halide composition was adjusted to manipulate the bandgap. The perovskites containing pure I, Br<sub>0.2</sub>I<sub>0.8</sub>, and Br<sub>0.4</sub>I<sub>0.6</sub> are notated as Br 0%, Br 20%, and Br 40%, respectively. To examine bandgaps of perovskite containing various Br ratios, absorbance and photoluminescence (PL) spectra were measured and their bandgaps were estimated using Tauc plot analysis. (Figure S1, Supporting Information) The spectra progressively blueshifted with an increase in Br species, attributed to the increasing optical bandgap of 1.55, 1.66, and 1.78 eV for Br 0%, Br 20%, and Br 40%, respectively. Moreover, the conduction band (CB) and valence band (VB) of the perovskites were also characterized with ultraviolet photoelectron spectroscopy (UPS) (Figure S2, Supporting Information), revealing that the energy levels within wider perovskite bandgaps shifted to lower energy states. Accordingly, through these integrated characterizations utilizing Tauc plot and UPS analysis, we can construct the energy band diagram of the perovskite-modified plasmonic Au/TiO<sub>2</sub>

nanodiode, depicted in Figure 1b. As Au has greater work function compared to perovskites and TiO<sub>2</sub>, two Schottky barriers are established at the interfaces, resulting in upward band bending within both perovskites and TiO<sub>2</sub>. When light impinges on the perovskite side, hot carriers are generated on both perovskite thin-layer and plasmonic Au nanostructure. The internal *E*-field and barrier heights at the Schottky junction interfaces allow hot carriers to be split, followed by hot-electron transfer to the TiO<sub>2</sub> layer. Given the electrical circuit connected between TiO<sub>2</sub> and plasmonic Au, the separated hot electrons flow toward external circuit as a steady-state photocurrent. The threshold photon energy required to generate hot-electron flow from the perovskites is estimated by the sum of the energy difference between the Fermi level and VB maximum of perovskites and the Schottky barrier height at the plasmonic Au/TiO<sub>2</sub> interface. Accordingly, we theoretically estimate that at least 2.3, 2.33, and 2.4 eV of photon energy is required for initiating hot-electron flux from Br 0%, Br 20%, and Br 40% perovskites, respectively. The morphology of the nanodiode was confirmed using scanning electron microscopy (SEM) and high-angle annular dark field–scanning transmission electron microscopy (HAADF–STEM), equipped with energy-dispersive X-ray spectroscopy (EDS), as shown in Figure 1c–e and S3, S4, Supporting Information, showing the plasmonic Au demonstrates connected islands morphology, and the spin-coated perovskite thin film is deposited uniformly as the topmost layer covering the plasmonic Au structure.

### 2.2. Hot-Electron Flow Dependency on the Perovskite Bandgap

To investigate the impact of perovskite bandgap on hot-electron flow, plasmonic Au nanodiodes were modified with perovskites with various bandgaps, followed by measuring both current–voltage (*I*–*V*) curves and short-circuit photocurrents. The thickness of the perovskite films was found to be ≈50 nm, as shown in Figure S5a, Supporting Information. We confirmed the nanodiodes exhibited rectifying behavior following the modification of the perovskite film under both dark and light illumination conditions (Figure 2a,b). Under dark conditions, we noted an open-circuit voltage (*V*<sub>OC</sub>) of +0.15 V for both bare and perovskite-modified plasmonic Au nanodiodes. However, upon exposure to light, the *V*<sub>OC</sub> of the bare plasmonic Au showed a negligible increase to +0.2 V, while that of perovskite-modified plasmonic diodes increases to +0.3 V. This suggests that the additional hot-electron flow from the perovskite contributes to enhancing the photovoltaic effect. It is noteworthy that the *V*<sub>OC</sub> of perovskite plasmonic Au nanodiodes remained equivalent despite differing bandgaps. This supports the idea that the band-bending flattening within perovskite layers, induced by hot-carrier excitation, is comparable across various bandgaps. Thus, we can achieve a consistent energetic driving force for splitting hot carriers following modification of the perovskite bandgap. As the hot electrons that surpass the Schottky barrier contribute to the steady-state photocurrent, we calculate the Schottky barrier heights at the plasmonic Au/TiO<sub>2</sub> interface using the thermionic emission model,<sup>[12]</sup> as shown in Figure S6, Supporting Information. Accordingly, we obtained the consistent Schottky barrier heights for all Br ratios, as indicated by Table S1 and Table S2, Supporting Information. Notably, even though the

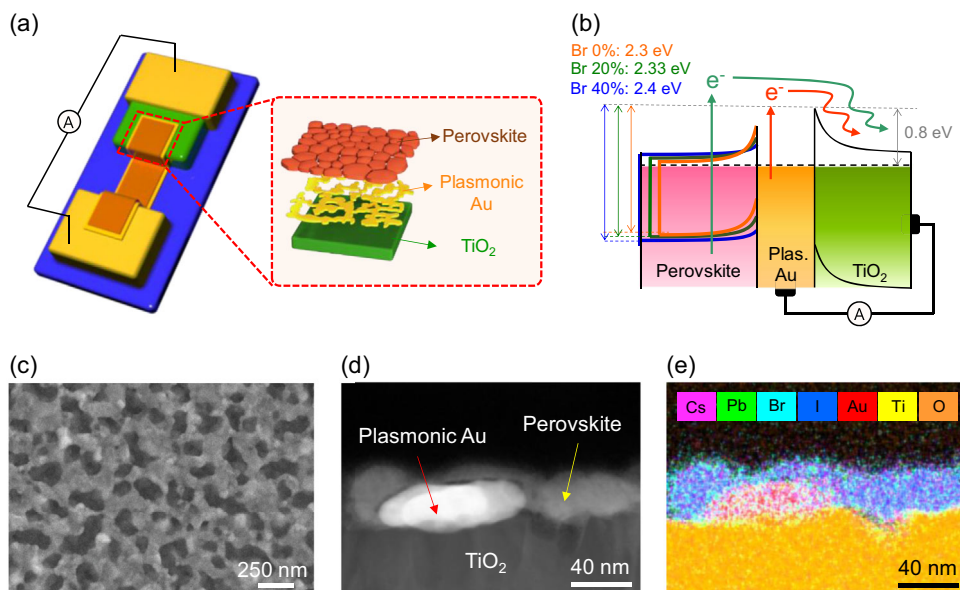


**Figure 1.** Characterization of the device structure. a) Scheme of the perovskite-modified plasmonic Au/TiO<sub>2</sub> nanodiode. b) Energy band diagram of plasmonic Au/TiO<sub>2</sub> nanodiodes modified with three different perovskite halide compositions. The halide site was changed from pure I to Br<sub>0.2</sub>I<sub>0.8</sub>, and Br<sub>0.4</sub>I<sub>0.6</sub>, which are noted as Br 0%, Br 20%, and Br 40%, respectively. c) Top-view SEM image, d) cross-sectional HAADF-STEM image, and e) EDS mapping images of the Br 40%/plasmonic Au/TiO<sub>2</sub> nanodiode.

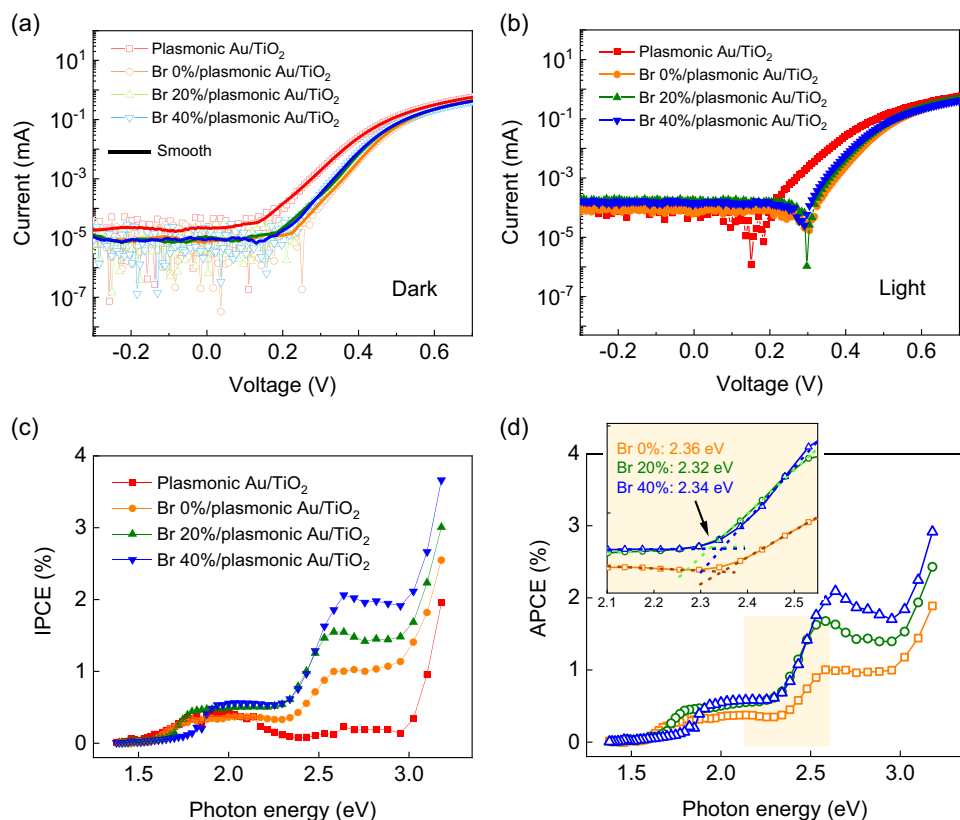


**Figure 2.** Hot-electron flow dependency on perovskite bandgap  $I$ - $V$  curves measured a) under dark and b) light irradiation. c) IPCE and d) APCE results measured on the perovskite-modified plasmonic Au nanodiodes. The inset in d) indicates zoomed-in APCE results of the yellow-colored highlighted region (2.1–2.5 eV) of the APCE results.

energetic driving force and Schottky barrier height for splitting hot carriers were comparable, the short-circuit photocurrent was increased from 97 to 141 nA when plasmonic Au was modified with wider perovskite bandgaps (Figure S5b, Supporting Information).

To address the origin of photocurrent enhancement in wider perovskite bandgap, IPCE of both bare and perovskite modified plasmonic Au nanodiodes was characterized (Figure 2c). In perovskite/plasmonic Au/TiO<sub>2</sub> nanodiode, hot-electron transport can be described through four pathways, as illustrated in Figure S7, Supporting Information. The bare plasmonic Au/TiO<sub>2</sub> indicates an IPCE peak centered at 1.88 eV, attributed to the plasmon-driven hot-electron flow from plasmonic Au (pathway 1), followed by an abrupt IPCE increase over 3.0 eV due to the band-to-band excitation in TiO<sub>2</sub>. When the perovskite film deposited on the plasmonic Au, the lateral Schottky interfaces between plasmonic Au and perovskite were created, facilitating the hot-electron transfer from plasmonic Au (pathway 2). Additionally, we confirmed that a slight increase in IPCE is occurring at  $\approx 1.6$ – $1.8$  eV, corresponding to the perovskite bandgap, as the thermalized hot electrons of perovskite pass directly to TiO<sub>2</sub> (pathway 3). Finally, sharp increases in IPCE above 2.3 eV are attributed to the hot-electron flow from the perovskite layer (pathway 4). It is noteworthy that the IPCE above 2.3 eV significantly increases in perovskite with higher Br ratios, highlighting the enhancement of hot-electron flux with wider perovskite bandgaps.

For a clearer evaluation of the threshold photon energy for initiating hot-electron flow from perovskite, we extracted absorbed photon-to-current efficiency (APCE) by normalizing IPCE with absorbance spectra (Figure S8, Supporting Information) to compare hot-electron injection efficiency in perovskite plasmonic nanodiodes with various bandgaps (Figure 2d). Notably, we found APCE was increased with higher Br ratios, indicating facilitated hot-electron injection with wider perovskite bandgap. The threshold photon energy for initiating hot-electron flow from the perovskite layer was determined from the point where two tangent lines drawn from both the low (<2.3 eV) and high (>2.3 eV) photon energy regions meet, as shown in the inset of Figure 2d. The experimentally observed threshold photon energies demonstrated  $\approx 2.3$ – $2.4$  eV, aligned well with the predicted values. In other words, modifying the perovskite bandgap does not significantly alter the threshold energy required for generating hot-electron flow in perovskite plasmonic nanodiodes, which is consistent with their comparable  $V_{OC}$  and Schottky barrier heights. Additionally, we demonstrate that despite the similar threshold energy, the hot-electron flow in the perovskite film increases with the widening of the perovskite bandgap. This underscores the necessity of understanding the underlying mechanism correlating hot-electron flow with perovskite bandgaps.

### 2.3. Hot-Electron Flow Dependency on Perovskite Film Thickness

To further investigate the contribution of perovskite hot-electron flow on the observed photocurrent enhancement, we examined the short-circuit photocurrent and IPCE on the plasmonic nanodiodes modified with various perovskite thicknesses of a fixed Br ratio (Br 20%). We hypothesize that if the thickness of perovskite exceeds the mean-free path of hot electrons, both the photocurrent

and IPCEs are expected to decrease. The perovskite film thicknesses were changed by adjusting the concentration of a perovskite precursor solution (Figure S9, Supporting Information). We observed that the short-circuit photocurrent was increased after depositing perovskite film, while it was reduced from 134 to 75 nA as the perovskite layer thicknesses increased from 50 to 75 nm (Figure 3a). Similarly, the IPCE of perovskite plasmonic nanodiodes was decreased with thicker perovskite films (Figure 3b).

The dependence of hot-electron flow on variations in perovskite thickness can be explained as Figure 3c. Upon irradiation, hot electrons are generated on both perovskite and plasmonic Au. When the perovskite layer is thicker than the mean-free path of hot electrons of the perovskites (16–90 nm),<sup>[19,20]</sup> the photocurrent is expected to decrease because the hot electrons undergo scattering within the perovskite layer before they reach the Schottky barrier at the interface between perovskite and plasmonic Au. Furthermore, a significant portion of the incident light will be absorbed in the perovskite, so less light will reach the plasmonic Au layer, resulting in reduced hot-electron generation on the plasmonic Au. These explanations are supported by the diminished plasmonic IPCE peak centered at 1.88 eV and the decreased IPCE in the high photon energy region (>2.3 eV) with increasing perovskite film thicknesses. The thermalized hot carriers within perovskites were detected at 1.66 eV, coincidence to its bandgap, attributed to the inherent junction formed between the perovskite and TiO<sub>2</sub> layer. However, their contribution to the overall IPCE is negligible, accounting for less than 0.5%. Moreover, the diffusion lengths of thermally equilibrated hot carriers in perovskites are estimated to be on the order of micrometers,<sup>[21]</sup> which is substantially larger than the perovskite films employed in this experiment. Therefore, the thermalized hot carriers cannot explain the observed decrease in IPCE with increasing perovskite thickness from 50 to 75 nm. These findings support that the observed photocurrents in the nanodiodes are primarily governed by the hot-electron flow originating from the perovskite, with a mean-free path less than 75 nm, in addition to hot-electron flow from plasmonic Au.

### 2.4. Hot-Electron Lifetime Dependency on Perovskite Bandgap

To clarify the mechanism behind the increased hot-electron flow in perovskite plasmonic Au nanodiodes with wider perovskite bandgaps, we investigated the hot-electron lifetimes using femtosecond TA experiments, which can track the ultrafast dynamics of hot carriers within the subpicosecond timescales. In TA experiments, samples were prepared on transparent quartz substrates instead of opaque single-side polished SiO<sub>2</sub> wafers to allow the pump and probe beams to penetrate, and the samples were excited at 420 nm with a fluence of  $55.7 \mu\text{J cm}^{-2}$  (see Supplementary Note 1, Supporting Information), where the halide phase segregation of perovskites can be ignored.<sup>[22]</sup> The TA spectra measured on Br 0%/plasmonic Au/TiO<sub>2</sub> structure at early time ranges (0.07–12.9 ps) and late time ranges (17–149 ps) are shown in Figure 4a,b, respectively. The TA data from bare plasmonic Au/TiO<sub>2</sub> and TiO<sub>2</sub> samples show less than one order or neglectable signal compared to the perovskite-modified samples (Figure S10, Supporting Information). Thus, we can regard

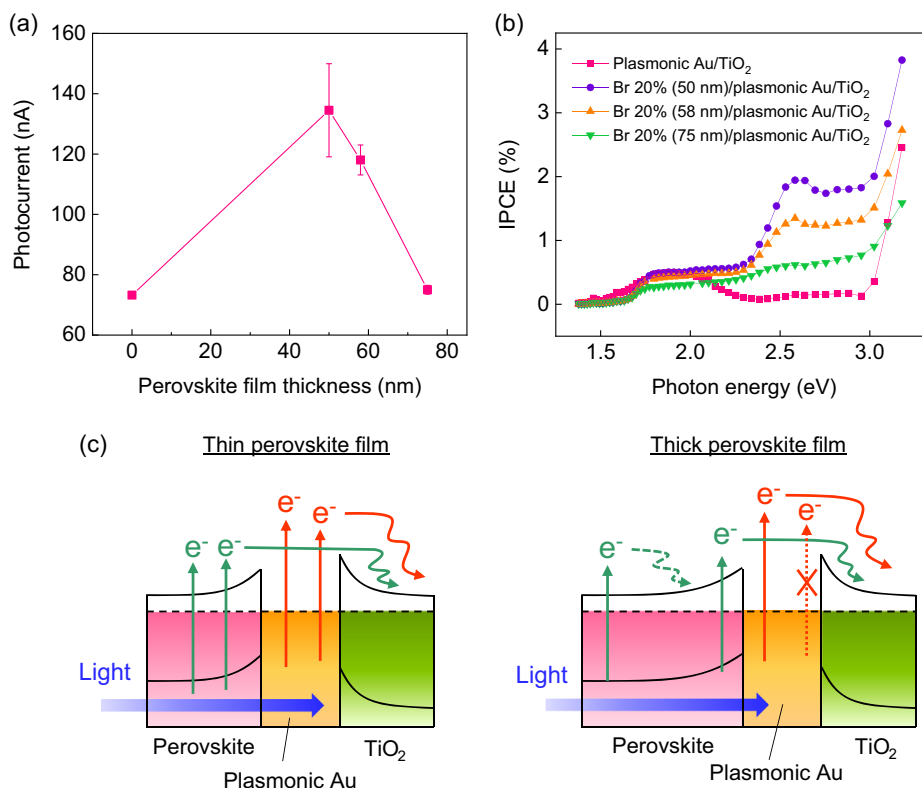


**Figure 3.** Hot-electron flow dependency on perovskite film thickness. a) Short-circuit photocurrents and b) IPCE results of the Br 20%/plasmonic Au/TiO<sub>2</sub> nanodiodes with various perovskite film thicknesses. c) Schematic illustration depicting the formation of hot-electron flow depending on the thickness of perovskite film.

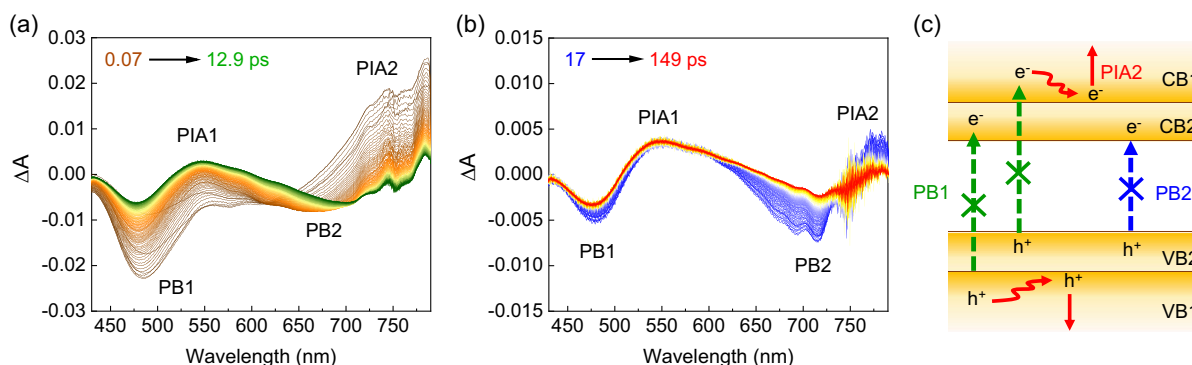


**Figure 4.** TA spectral features of the perovskite. TA spectra measured on the Br 0%/plasmonic Au/TiO<sub>2</sub> structure at a) early time ranges (0.07–12.9 ps) and b) late time ranges (17–149 ps). The sample was excited at 420 nm with a fluence of 55.7 μJ cm<sup>-2</sup>. c) Illustration depicting the origin of the spectral features observed in the acquired TA spectra.

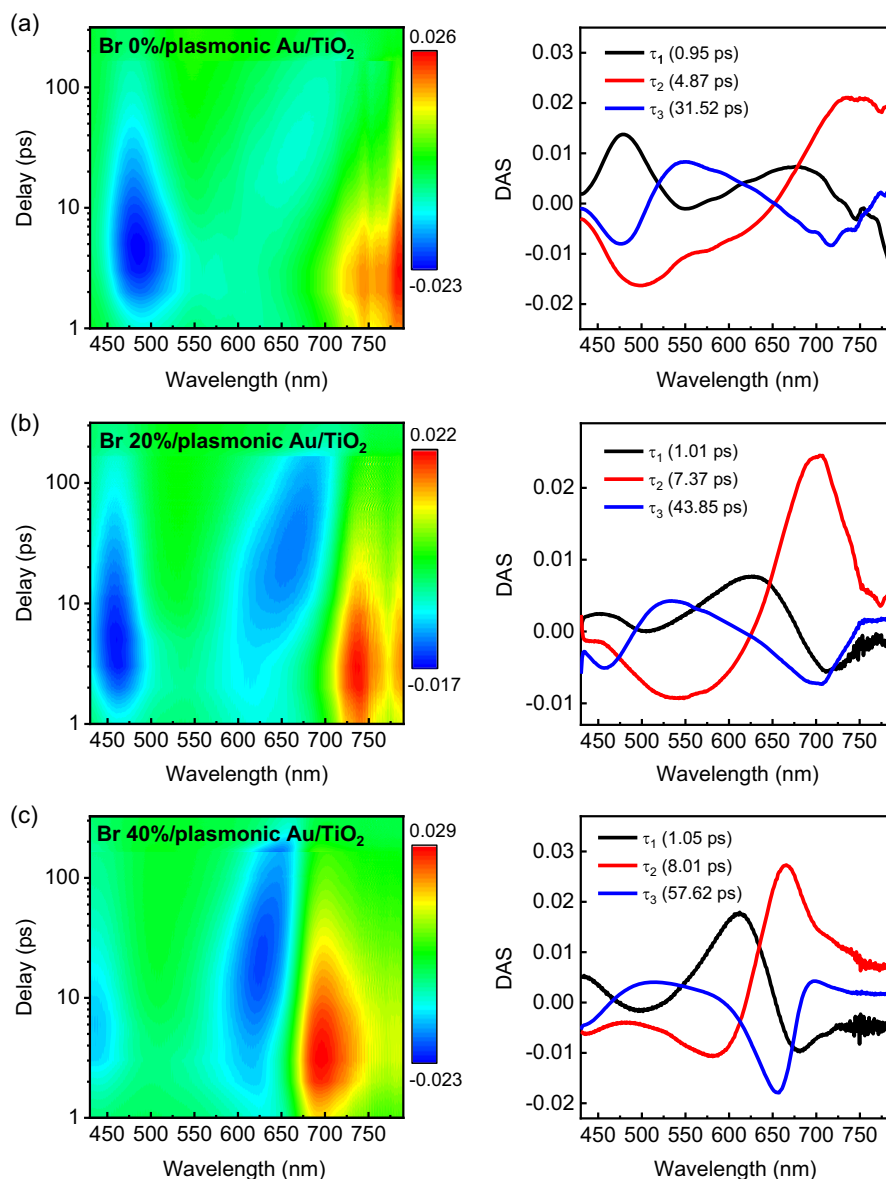
the observed TA spectra from the perovskite-modified samples as governed by carrier dynamics within the perovskites. Generally, four typical features are shown in perovskite samples in the visible light region, including two negative photobleaching (PB) peaks and two positive photoinduced absorption (PIA) peaks.<sup>[7,23]</sup> The Br 0% sample shows two PB peaks at 483 and 661 nm and two PIA peaks at 550 and 786 nm, which are notated as PB1, PB2, PIA1, and PIA2, respectively. A detailed explanation for carrier dynamics related to the observed spectral features is illustrated in

Figure 4c. The negative PB peaks are generated due to the depletion of ground-state carriers. As perovskites are known to have dual VB and CB, the carriers excited from a deeper VB to a CB edge or from a VB edge to a higher CB state contribute to PB1, and the excitation from a VB edge to a CB edge is related to PB2. Considering the origin of the PB2 signal, the PB2 peak should be centered at the bandgap energy of Br 0% (800 nm). However, the PB2 peak of Br 0% sample was observed around 620 nm in the early times and then gradually redshifted with time. The spectral

shifts occur because carrier accumulation within the perovskite results in increased intrinsic bandgap in the early times, known as Burstein–Moss shift, which commonly appears in high fluence pump pulse.<sup>[24]</sup> On the other hand, PIA1 results from photoinduced reflectivity change within the perovskite, rather than carrier dynamics,<sup>[25]</sup> and PIA2 originates from the excitation of hot carriers to the higher states.<sup>[23]</sup> Thus, we attribute the decay of the PIA2 peak to hot-carrier relaxation dynamics.

In **Figure 5**, TA spectra of the perovskite-modified plasmonic Au nanodiodes are shown in the left panels, and they all indicate four distinctive spectral features of the perovskites. As shown in the TA spectra, the negative absorption bands corresponding to PB1 in the 400–550 nm and PB2 in the 600–700 nm are blueshifted with an increased Br ratio, due to the increased

perovskite bandgap. To quantitatively explore hot-carrier relaxation dynamics, we conducted global analysis, where spectrally invariant decay components are fit to the entire transient map with multiexponential functions. All decay profiles can be expressed by tetra-exponential functions with shared four relaxations times, as shown in **Table 1**. We suggest the longest time component ( $\tau_4$ ) corresponds to the lifetime of carriers at the band edges.<sup>[26,27]</sup> As it is out of the time range covered in our experiment, it is not taken into account in the following discussion. To accurately assign the origin of the time constants, we extracted decay-associated spectra (DAS) from the TA spectra of the perovskite-modified plasmonic Au nanodiodes. To extract DAS, all decay profiles ( $I(\lambda, t)$ ) monitored at all wavelengths were fitted with the following equation:



**Figure 5.** Ultrafast hot-electron dynamics of the perovskites. Pseudo-color TA spectra (left panel) and DAS (right panel) for a) Br 0%/plasmonic Au/TiO<sub>2</sub>, b) Br 20%/plasmonic Au/TiO<sub>2</sub>, and c) Br 40%/plasmonic Au/TiO<sub>2</sub>. DAS spectra were derived by conducting a global analysis of the TA spectra.

**Table 1.** Summarized fit parameters for the multiexponential decay of the perovskite/plasmonic Au/TiO<sub>2</sub> structures with three various Br ratios.

	$\tau_1$ [ps]	$\tau_2$ [ps]	$\tau_3$ [ps]	$\tau_4$ [ps]
Br 0%/plasmonic Au/TiO <sub>2</sub>	0.95 ± 0.01	4.87 ± 0.06	31.52 ± 0.27	>2000
Br 20%/plasmonic Au/TiO <sub>2</sub>	1.01 ± 0.01	7.37 ± 0.10	43.85 ± 0.55	>2000
Br 40%/plasmonic Au/TiO <sub>2</sub>	1.05 ± 0.02	8.01 ± 0.12	57.62 ± 1.58	>2000

$$I(\lambda, t) = \sum_i^n \alpha_i(\lambda) \exp\left(-\frac{t}{\tau_i}\right) \quad (1)$$

where  $i$  is the index of decay components,  $\tau_i$  is the exponential time constant of each decay component shown in Table 1, and  $\alpha_i$  is the amplitude of each decay component. The DAS for perovskite-modified plasmonic Au nanodiodes are presented in the right panels of Figure 5.

We observed that the DAS for the fastest constant ( $\tau_1$ ) indicate two positive peaks around ground-state bleaching (GSB) and negative or negligible signals at PIA bands. These features are fingerprints of the trap-assisted hot-carrier relaxation.<sup>[28]</sup> As we utilized polycrystalline perovskite thin films, it is natural that carriers are trapped at grain boundaries within subpicoseconds, attributing the dynamics of  $\tau_1$  to carrier trapping. The DAS for the second constant ( $\tau_2$ ) exhibit GSB peaks in parallel with a strong PIA2 band, implying the depopulation of ground-state carriers and the existence of hot carriers. Therefore,  $\tau_2$  can be associated with hot-carrier relaxation lifetime. Finally, the DAS for the third constant ( $\tau_3$ ), showing two GSB peaks, suggests the occurrence of Auger recombination of biexcitons,<sup>[27]</sup> implying that  $\tau_3$  represents the lifetime of biexcitons in perovskites. Considering that the hot-carrier density in our TA experiment is estimated to be  $1.18 \times 10^{19} \text{ cm}^{-3}$  (see Supplementary Note 2, Supporting Information), it is possible to observe Auger recombination, a phenomenon typically manifesting at high hot-carrier densities ( $>10^{19} \text{ cm}^{-3}$ ).<sup>[7,20]</sup> As the lifetime of biexcitons is shorter than free carriers,<sup>[29]</sup> Auger recombination ( $\tau_3$ ) occurs more rapidly than band-to-band recombination ( $\tau_4$ ). All four time constants

we obtained were similar to those reported in other literature,<sup>[7,12,27]</sup> supporting our discussions.

Accordingly, we propose the hot-electron relaxation mechanisms in perovskite as shown in Figure 6a. Our model was further validated by conducting the kinetic analysis on the TA spectra of three perovskite/plasmonic Au/TiO<sub>2</sub> structures with different perovskite bandgaps (see Supplementary Note 3, Supporting Information). Figure S11–S13, Supporting Information compare the experimental TA spectra with the theoretical TA spectra calculated using a kinetic model that incorporates the proposed hot-electron mechanisms, along with the residuals between the two TA spectra. We observed that the residuals between the experimental and best-fitted TA spectra for three perovskite plasmonic structures are featureless and relatively small, indicating that the measured TA spectra for three perovskites are well represented by a linear combination of the three species-associated difference spectrum curves (Figure S11b–S13b, Supporting Information).

## 2.5. Mechanism of the Variation in Hot-Electron Lifetime Due to Perovskite Bandgap Modification

Consequently, we observed an extended hot-carrier lifetime ranging from 4.87 to 8.01 ps with wider perovskite bandgaps. Previous experimental and theoretical literature has established a correlation between hot-carrier lifetime and perovskite halide composition, particularly in terms of changes in phonon dispersion. As the number of phonons is influenced by the electronic structure determined by lattice parameters, it is plausible that halide substitution modifies the hot-carrier lifetime.<sup>[30]</sup> Indeed, it has been revealed that changing the halide composition from I to Br results in a decreased lattice constant, causing a shift in crystal structure from tetragonal to pseudocubic. This crystal structure change results in the expansion of electronic density of states, improving phonon propagation and facilitating hot-carrier relaxation.<sup>[11,31,32]</sup>

However, our observation presents a trend that differs from these results. This is because FA-rich perovskites with pure iodine already exhibit a cubic phase at room temperature.<sup>[33]</sup>

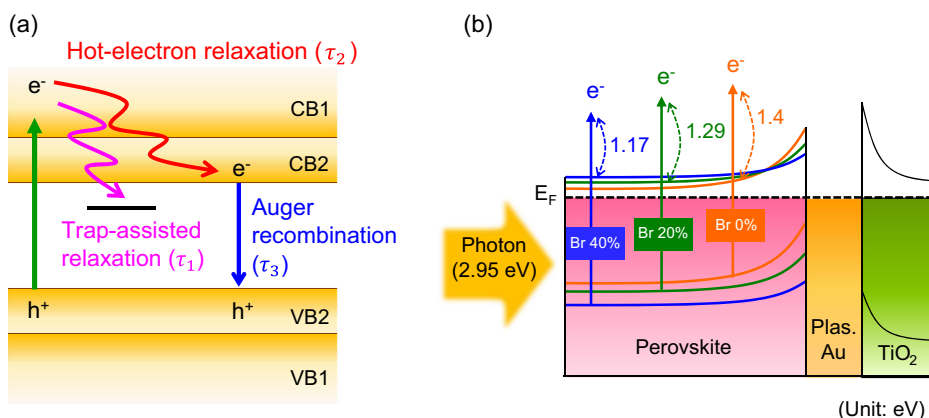


**Figure 6.** Correlation between hot-electron lifetime and flow. a) Schematic of kinetic model including various possible hot-electron relaxation mechanisms within perovskite film. b) Illustration showing the maximum excessive energy of hot electrons excited with an incident photon energy of 2.95 eV (420 nm) on perovskite films with three different Br ratios.

Additionally, in our experiment, we introduced Br species to I-rich perovskites, reaching up to 40% of the mixture to prevent phase segregation. This partial mixing of Br is expected to alter the lattice parameter by  $\approx 0.1\text{--}0.2\text{ \AA}$ .<sup>[34,35]</sup> Indeed, the lattice parameter of the perovskite with Br 20% was decreased from 8.89 to 8.78 Å as we added an additional 20% of Br species (Br 40%) (Figure S14, Supporting Information). Thus, we suggest that while the lattice parameters of our perovskites may slightly decrease with higher Br contents, these structural changes have negligible effects on reducing hot-carrier lifetimes. Instead, we attribute the extended hot-carrier lifetime in perovskites with wider bandgaps to reduced carrier-carrier interactions during the hot-electron relaxation process. When the perovskites are excited with a pump beam energy of 2.95 eV, a perovskite with wider bandgap generates a lower excess energy for hot electrons, specifically 1.4, 1.29, and 1.17 eV for Br 0%, Br 20%, and Br 40%, respectively, as depicted in Figure 6b. As the hot-carrier scattering rate in perovskite is likely to be enhanced with a higher excess energy above the bandgap,<sup>[36]</sup> it is possible to address that the perovskites generating lower excess energy of hot electrons result in a longer hot-electron lifetime. In other words, widening the perovskite bandgap by increasing the Br ratio allows the generation of hot carriers with lower excess energy, resulting in a slower hot-carrier scattering rate and an extended hot-carrier lifetime.

To gain further insight into the hot-electron injection within the perovskite/Au/TiO<sub>2</sub> structure, we conducted control TA experiments on perovskite/TiO<sub>2</sub> samples (Figure S15, Supporting Information), where hot electrons are fully thermalized to the CB edge of the perovskite. The determined time constants are summarized in Table S3, Supporting Information. Consequently, we noted a decrease in the hot-electron lifetime ( $\tau_2$ ) in the presence of a plasmonic Au structure. As the hot-electron lifetime decreases when they are partially injected into acceptor layers,<sup>[37]</sup> this reduced hot-electron lifetime of perovskite in the presence of plasmonic Au highlights the successful injection of hot electrons from perovskite to plasmonic Au/TiO<sub>2</sub> before relaxation. Incidentally, it is worth noting that the influence of hot-electron flux due to the degradation of perovskite materials is a crucial factor in determining the application of perovskite hot-electron solar cells,<sup>[38]</sup> representing an intriguing avenue for future research.

### 3. Conclusion

In conclusion, we demonstrated the extension of hot-electron lifetime and enhancement of hot-electron flux in the perovskite-modified plasmonic Au/TiO<sub>2</sub> nanodiodes by tuning the perovskite bandgap. The systematic control of the bandgap was accomplished by varying the ratio of Br/I, resulting in a tunable bandgap ranging from 1.55 to 1.78 eV with increased Br species. We found that plasmonic Au nanodiodes modified with wider perovskite bandgaps exhibit enhanced photocurrents and IPCE due to the increased hot-electron flow from the perovskite layers. The underlying mechanism behind the enhanced hot-electron flow with a wider perovskite bandgap was elucidated by femtosecond TA spectroscopy and attributed to the extended hot-carrier lifetime from 4.87 to 8.01 ps with wider perovskite bandgaps. We suggest this prolonged

hot-electron lifetime with wider bandgaps is ascribed to reduced carrier-carrier scattering rate, stemming from the excitation of hot electrons with lower excess energy in the perovskite. These findings underscore the importance of perovskite bandgap engineering for finely tuning the hot-carrier behavior, including the modulation of excess energy, to extend their lifetime and enhance their flow. We believe this comprehensive exploration of engineering hot-carrier physics-for-functionality holds promise for advancing the development of next-generation hot-carrier devices.

### 4. Experimental Section

**Sample Preparation:** Perovskite-modified plasmonic Au/TiO<sub>2</sub> nanodiodes were fabricated following the previously reported method.<sup>[12]</sup> First, TiO<sub>2</sub> film (240 nm) was generated on a SiO<sub>2</sub> substrate, where 300 nm of SiO<sub>2</sub> was thermally grown on a Si wafer, by annealing a Ti layer (140 nm). Then, Ti (45 nm) and Au (100 nm) were evaporated consecutively at the ends of the device to create ohmic electrode pads. The plasmonic Au layer was fabricated by annealing a thin-film Au layer (15 nm) at 240 °C for 40 min. To make a perovskite layer, the perovskite solutions were prepared by dissolving FAI (Greatcell Solar), FABr (Greatcell Solar), MABr (Greatcell Solar), CsI (Sigma-Aldrich), PbI<sub>2</sub> (TCI Chemicals), and PbBr<sub>2</sub> (TCI Chemicals) precursors with the target composition to form stoichiometric (FA<sub>0.65</sub>MA<sub>0.20</sub>CS<sub>0.15</sub>)Pb(I<sub>1-x</sub>Br<sub>x</sub>)<sub>3</sub>, X = 0, 0.2, and 0.4, in DMF (Sigma-Aldrich)/NMP (Sigma-Aldrich) mixed solvent (DMF: NMP = 4:1 volume ratio). The prepared solution was spin-coated on the plasmonic Au/TiO<sub>2</sub> substrate at 4000 rpm for 20 s. Subsequently, the spin-coated film was then immersed in a diethyl ether antisolvent bath for 30 s to form a crystalline phase. After a diethyl ether bathing, the film was annealed at 100 °C for 10 min. All film preparation procedures were conducted in a nitrogen-filled glove box.

**Characterization and Measurement:** To analyze the morphology and elemental distribution of the devices, an SEM (Hitachi SU5000) and a TEM (Talos F200X) with EDS were utilized. Additionally, a focused ion beam (FEI Helios Nanolab 450 F1) milling process was employed to prepare the TEM sample. The energy levels of perovskite were characterized using an UPS (Kratos Axis-Supra) using He (I) source (21.2 eV), with a bias voltage of -10 eV. The photoelectron binding energy was calibrated using the Fermi edge of sputtered Au film. The photoelectrical performances of the device were measured with a source meter unit (Keithley 2400) with a tungsten-halogen lamp (9 mW cm<sup>-2</sup>) as the light source. A tunable light source (Newport, TLS-300XU) was employed to conduct the IPCE measurement. A pump-probe TA spectroscopy was utilized to measure the femtosecond time-resolved absorption spectra. The samples were prepared on visibly transparent quartz glass, instead of a thermally grown SiO<sub>2</sub> on a Si wafer, for conducting TA spectra. The output pulses at a wavelength of 800 nm from Ti:sapphire amplified laser (Coherent, Legend Elite) were divided to generate the pump and probe beams. The laser pulses in the pump arm are converted to a pump beam of 420 nm (2.95 eV) using an optical parametric amplifier (Light Conversion, TOPAS prime), while another part of the fundamental laser pulses was directed at a 1 mm path length quartz cell containing water to generate a white light continuum for the probe beam. The white light was then transmitted through the sample cell with a 2.0 mm optical path, and the transmitted light was detected using a CCD detector installed in the absorption spectroscopy system with controlled optical delay.

### Supporting Information

Supporting Information is available from the Wiley Online Library or from the author.

## Acknowledgements

Y.P., J.C. and D.K. contributed equally to this work. This work was supported by the National Research Foundation of Korea (NRF) grant funded by the Korean government (MSIT) (grant no. 2022R1A2C3004242), Institute for Basic Science (IBS) (IBS-R033). Y.P. specially acknowledges POSCO Science Fellowship awarded by POSCO TJ Park Foundation.

## Conflict of Interest

The authors declare no conflict of interest.

## Author Contributions

**Yujin Park:** designed the project and carried out the device fabrication and characterization. **Daehan Kim:** synthesized and characterized the perovskite materials. **Jungkweon Choi** and **Dae Won Cho:** performed transient absorption experiments. **Jungmin Kim, Yujin Roh,** and **Hyunhwa Lee:** contributed to the scientific discussions. **Hyotcherl Ihee, Byungha Shin,** and **Jeong Young Park:** supervised the project. All authors contributed to the preparation of the manuscript.

## Data Availability Statement

The data that support the findings of this study are available from the corresponding author upon reasonable request.

## Keywords

bandgap tuning, hot electrons, localized surface plasmon resonance, perovskites, photodetection

Received: July 6, 2024

Revised: July 22, 2024

Published online:

- [1] M. W. Knight, H. Sobhani, P. Nordlander, N. J. Halas, *Science* **2011**, 332, 702.
- [2] W. Li, Z. J. Coppens, L. V. Besteiro, W. Y. Wang, A. O. Govorov, J. Valentine, *Nat. Commun.* **2015**, 6, 8379.
- [3] D. Sun, G. Aivazian, A. M. Jones, J. S. Ross, W. Yao, D. Cobden, X. D. Xu, *Nat. Nanotechnol.* **2012**, 7, 114.
- [4] R. G. Li, W. H. Cheng, M. H. Richter, J. S. DuChene, W. M. Tian, C. Li, H. A. Atwater, *ACS Energy Lett.* **2021**, 6, 1849.
- [5] Y. Negrín-Montecelo, A. Movsesyan, J. Gao, S. Burger, Z. M. M. Wang, S. Nlate, E. Pouget, R. Oda, M. Comesaña-Hermo, A. O. Govorov, M. A. Correa-Duarte, *J. Am. Chem. Soc.* **2022**, 144, 1663.
- [6] K. Song, H. Lee, M. Lee, J. Y. Park, *ACS Energy Lett.* **2021**, 6, 1333.
- [7] M. Li, J. Fu, Q. Xu, T. C. Sum, *Adv. Mat.* **2019**, 31, 1802486.
- [8] S. W. Lee, H. Lee, Y. Park, H. Kim, G. A. Somorjai, J. Y. Park, *Surf. Sci. Rep.* **2021**, 76, 100532.
- [9] H. Lee, H. Lee, J. Y. Park, *Nano Lett.* **2019**, 19, 891.
- [10] H. Lee, K. Song, M. Lee, J. Y. Park, *Adv. Sci.* **2020**, 7, 2001148.
- [11] S. Kahmann, M. A. Loi, *J. Mater. Chem. C* **2019**, 7, 2471.
- [12] Y. Park, J. Choi, C. Lee, A. N. Cho, D. W. Cho, N. G. Park, H. Ihee, J. Y. Park, *Nano Lett.* **2019**, 19, 5489.
- [13] Y. Park, J. Choi, M. Kang, H. Lee, H. Ihee, J. Y. Park, *J. Phys. Chem. C* **2021**, 125, 2575.
- [14] Q. C. Gu, C. H. Hu, J. M. Yang, J. T. Lv, Y. Ying, X. X. Jiang, G. Y. Si, *Mater. Des.* **2021**, 198, 109374.
- [15] P. L. Zhang, G. B. Zhu, Y. Shi, Y. P. Wang, J. H. Zhang, L. C. Du, D. J. Ding, *J. Phys. Chem. C* **2018**, 122, 27148.
- [16] J. S. Chen, M. E. Messing, K. B. Zheng, T. Pullerits, *J. Am. Chem. Soc.* **2019**, 141, 3532.
- [17] H. Lee, P. Boonmongkolras, S. Jun, D. Kim, Y. Park, J. Koh, Y.-H. Cho, B. Shin, J. Y. Park, *ACS Appl. Energy Mater.* **2023**, 6, 1565.
- [18] D. Kim, H. J. Jung, I. J. Park, B. W. Larson, S. P. Dunfield, C. X. Xiao, J. Kim, J. H. Tong, P. Boonmongkolras, S. G. Ji, F. Zhang, S. R. Pae, M. Kim, S. B. Kang, V. Dravid, J. J. Berry, J. Y. Kim, K. Zhu, D. H. Kim, B. Shin, *Science* **2020**, 368, 155.
- [19] M. J. Li, S. Bhaumik, T. W. Goh, M. S. Kumar, N. Yantara, M. Gratzel, S. Mhaisalkar, N. Mathews, T. C. Sum, *Nat. Commun.* **2017**, 8, 14350.
- [20] I. Dursun, P. Maity, J. Yin, B. Tuređi, A. A. Zhumekenov, K. J. Lee, O. F. Mohammed, O. M. Bakr, *Adv. Energy Mater.* **2019**, 9, 1900084.
- [21] S. D. Stranks, G. E. Eperon, G. Grancini, C. Menelaou, M. J. P. Alcocer, T. Leijtens, L. M. Herz, A. Petrozza, H. J. Snaith, *Science* **2013**, 342, 341.
- [22] S. Draguta, O. Sharia, S. J. Yoon, M. C. Brennan, Y. V. Morozov, J. M. Manser, P. V. Kamat, W. F. Schneider, M. Kuno, *Nat. Commun.* **2017**, 8, 200.
- [23] Z. Guo, Y. Wan, M. J. Yang, J. Snaider, K. Zhu, L. B. Huang, *Science* **2017**, 356, 59.
- [24] J. S. Manser, P. V. Kamat, *Nat. Photonics* **2014**, 8, 737.
- [25] M. B. Price, J. Butkus, T. C. Jellicoe, A. Sadhanala, A. Briane, J. E. Halpert, K. Broch, J. M. Hodgkiss, R. H. Friend, F. Deschler, *Nat. Commun.* **2015**, 6, 8420.
- [26] L. T. Dou, A. B. Wong, Y. Yu, M. L. Lai, N. Kornienko, S. W. Eaton, A. Fu, C. G. Bischak, J. Ma, T. N. Ding, N. S. Ginsberg, L. W. Wang, A. P. Alivisatos, P. D. Yang, *Science* **2015**, 349, 1518.
- [27] K. B. Zheng, K. Zidek, M. Abdellah, J. S. Chen, P. Chabera, W. Zhang, M. J. Al-Marri, T. Pullerits, *ACS Energy Lett.* **2016**, 1, 1154.
- [28] S. Narra, E. Jokar, O. Pearce, C. Y. Lin, A. Fathi, E. W. G. Diau, *J. Phys. Chem. Lett.* **2020**, 11, 5699.
- [29] R. Ahumada-Lazo, R. Saran, O. Woolland, Y. P. Jia, M. E. Kyriazi, A. G. Kanaras, D. Binks, R. J. Curry, *J. Phys. Photonics* **2021**, 3, 021002.
- [30] T. Debnath, D. Sarker, H. Huang, Z. K. Han, A. Dey, L. Polavarapu, S. V. Levchenko, J. Feldmann, *Nat. Commun.* **2021**, 12, 2629.
- [31] H. Chung, S. Il Jung, H. J. Kim, W. Cha, E. Sim, D. Kim, W. K. Koh, J. Kim, *Angew. Chem. Int. Ed.* **2017**, 56, 4160.
- [32] E. M. Talbert, H. F. Zarick, A. Boulesbaa, N. Soetan, A. A. Puzosky, D. B. Geohegan, R. Bardhan, *Nanoscale* **2017**, 9, 12005.
- [33] T. A. S. Doherty, S. Nagane, D. J. Kubicki, Y. K. Jung, D. N. Johnstone, A. N. Iqbal, D. Y. Guo, K. Frohna, M. Danaie, E. M. Tennyson, S. Macpherson, A. Abfalterer, M. Anaya, Y. H. Chiang, P. Crout, F. S. Ruggieri, S. Collins, C. P. Grey, A. Walsh, P. A. Midgley, S. D. Stranks, *Science* **2021**, 374, 1598.
- [34] M. E. Calvo, *J. Mater. Chem. A* **2017**, 5, 20561.
- [35] L. K. Ono, E. J. Juarez-Perez, Y. B. Qi, *ACS Appl. Mater. Interfaces* **2017**, 9, 30197.
- [36] J. M. Richter, F. Branchi, F. V. D. Camargo, B. D. Zhao, R. H. Friend, G. Cerullo, F. Deschler, *Nat. Commun.* **2017**, 8, 376.
- [37] D. C. Ratchford, A. D. Dunkelberger, I. Vurgaftman, J. C. Owrutsky, P. E. Pehrsson, *Nano Lett.* **2017**, 17, 6047.
- [38] J. I. J. Choi, M. E. Khan, Z. Hawash, K. J. Kim, H. Lee, L. K. Ono, Y. Qi, Y.-H. Kim, J. Y. Park, *J. Mater. Chem. A* **2019**, 7, 20760.